Case Studies in Construction Materials 17 (2022) e01320

Contents lists available at ScienceDirect

Case Studies in Construction Materials

journal homepage: www.elsevier.com/locate/cscm

Insight into the microstructural and durability characteristics of 3D printed concrete: Cast versus printed specimens

Pawel Sikora [a,*], Mateusz Techman [a], Karol Federowicz [a], Ahmed M. El-Khayatt [b,c], H.A. Saudi [d], Mohamed Abd Elrahman [e], Marcin Hoffmann [f], Dietmar Stephan [g], Sang-Yeop Chung [h,**]

[a] Faculty of Civil and Environmental Engineering, West Pomeranian University of Technology in Szczecin, Poland
[b] Department of Physics, College of Science, Imam Mohammad Ibn Saud Islamic University, (IMSIU), Riyadh, Saudi Arabia
[c] Reactor Physics Department, Nuclear Research Centre, Atomic Energy Authority, 13759 Cairo, Egypt
[d] Department of Physics, Faculty of Science, Al-Azhar University, Women Branch, Nasr City, Cairo, Egypt
[e] Structural Engineering Department, Mansoura University, Mansoura City 35516, Egypt
[f] Faculty of Mechanical Engineering and Mechatronics, West Pomeranian University of Technology in Szczecin, Poland
[g] Building Materials and Construction Chemistry, Technische Universität Berlin, Germany
[h] Department of Civil and Environmental Engineering, Sejong University, Seoul 05006, Republic of Korea

ARTICLE INFO

Keywords:
3D printing
Additive manufacturing
Concrete
Microstructure
Durability
Micro-CT

ABSTRACT

This study presents the comparison of microstructural and durability characteristics of 3D printed concrete (3DPC) depending on its production method (printing or casting). Printed samples with different numbers of layers, as well as a cast specimen with an identical mix composition, were produced and compared, with their microstructural pore and solid characteristics quantitatively and qualitatively investigated. For this purpose, scanning electron microscopy (SEM), mercury intrusion porosimetry (MIP) and X-ray micro-computed tomography (micro-CT) were utilized to evaluate the microstructures of the 3DPC. In particular, quantitative approaches using micro-CT data were newly proposed for a better understanding of the microstructural characteristics of 3DPC. Moreover, their durability-related characteristics and transport properties, including freeze-thaw and thermal resistance, were examined and compared. Despite noticeable differences between the microstructures of the printed and cast specimens, including their anisotropic and inter-layer porosity and heterogeneity, confirmed by MIP, SEM and micro-CT, no significant differences in the transport (capillary water porosity and water sorptivity) or durability-related properties (frost and thermal attack) were found. This was due to the dense and homogenous microstructure of 3DPC, which is attributable to the high binder content and low w/b of the mixture. Moreover, the newly proposed evaluation provided reasonable quantitative and qualitative characteristics, which can be used to demonstrate and predict the material properties of 3DPC.

* Corresponding author at: Faculty of Civil and Environmental Engineering, West Pomeranian University of Technology in Szczecin, Szczecin, Poland.
** Corresponding author.
E-mail addresses: pawel.sikora@zut.edu.pl (P. Sikora), sychung@sejong.ac.kr (S.-Y. Chung).

https://doi.org/10.1016/j.cscm.2022.e01320
Received 16 May 2022; Received in revised form 5 July 2022; Accepted 15 July 2022
Available online 16 July 2022

1. Introduction

In the last decade, the use of 3D printed concrete (3DPC) has been widely established in the construction community, with the first industrial applications already available. Additive manufacturing (AM) is a key pillar of Industry 4.0 and thus substantial research interest is being put into it, to develop novel and sustainable solutions for printable cementitious composites.

There are many fields where 3DPC can be applied: from simple housing projects to complex engineering structures, such as bridges and architectural facades or protective structures and lunar applications [1,2]. It is widely agreed that 3D printing technology of concrete offers manifold of benefits when compared to conventional concrete. First of all, AM technology allows formwork-free construction, thus dramatic reduction in project costs can be achieved. Moreover, printing technology lowers the amount of wastes generated during structure construction, thus reducing the environmental impacts of the construction process. Finally, due to the continuous work of the printer the project time can be shortened with less labor force required [3].

3D printed mixture compositions differ significantly from conventional concrete, as they are composed mostly of fine fractions. 3DPC is composed mainly of binder, fine aggregates and chemical admixtures, with only a limited amount of coarse aggregate introduced into the mixture (if any). This in turn results in substantially different durability and mechanical performances than conventional concrete mixtures [4,5].

Although there have been substantial developments in the field of 3DPC, the production of 3D printed structures requires a thorough understanding of elements' behavior, as their performance is quite different to that of pre-cast or monolithic concrete elements. Even though the evaluation techniques for 3DPC performance have still not been standardized, there is widespread agreement that printed specimens should be evaluated in relation to mold-cast samples. The microstructural characteristics of mold-cast specimens differ from that of 3D printed ones [6–8].

The printing process consists of pressure-pumping and deposition, while cast specimens are placed into formwork and vibrated so as to remove entrapped air, resulting in discrepancies in the microstructural characteristics of the specimens produced. In addition, the deposition of subsequent layers results in substantial differences between the porosities of the core part of the layer and near the interlayer connection, with this latter area thus widely considered to be a "weak chain" in the mechanical performance of 3DPC [9–12]. Similarly, other studies have reported weak interlayer zones which may allow intense capillary suction and the ingress of harmful substances into the concrete, thus increasing the corrosion rate of 3DPC [13,14].

Various microstructural evaluating techniques are typically used to assess mechanisms related to the mechanical and durability performances of 3D printing elements. These include scanning electron microscopy (SEM), optical microscopy, mercury intrusion porosimetry (MIP) and 2D image evaluation techniques. Unfortunately, microscopic evaluations are limited only to flat surface evaluations, while volumetric ones are rarely performed. The MIP technique is very effective in evaluating pore characteristics, but has limited size determination, making it impossible to determine larger air voids [15]. X-ray micro-computed tomography (micro-CT) is therefore often applied to complement the various imagining techniques [16,17]. It makes it possible to perform non-destructive qualitative determination of printed elements, so as to evaluate their volumetric characteristics. This is very important, as the printing process results in significant pore anisotropy (directional dependence) [18,19].

Micro-CT is utilized for qualitative and quantitative evaluations of printed elements [6,7,20,21]. For instance, it has been used to evaluate the aggregate distribution and potential buildability of a mixture, as well as to determine the steel fiber orientation in a mixture [22–24]. Recently, Chougan et al. [18] conducted a comparative study of both micro-CT and 2D standardized image-analysis methods, showing a good correlation in the results obtained, as well as indicating that both techniques can be coupled for effective specimen evaluation.

A comprehensive study conducted by Kruger et al. [7] has shown significant differences between the microstructural porosities of 3D printed and cast concrete. Concurring conclusions were drawn by Chen et al. [25] where printed specimen microstructures were evaluated. In addition, the studies performed by Sikora et al. [19] and Chougan et al. [18] have confirmed an alignment of pores along the printing direction, assessed in terms of lineal-path function.

Although several studies have been performed on the material aspects of 3D printed concrete, most of them have focused on macroscopic characteristics, such as total and local porosity. A deeper examination of microstructural characteristics is necessary to understand the properties of printed materials, including their mechanical performance and durability. Knowledge regarding the interlayer connection, as well as bulk characteristics, will help to improve the durability of 3D printed elements; especially those exposed to severe environmental conditions including freezing and thawing cycles.

This paper thus aims to evaluate the microstructural characteristics (SEM, MIP, micro-CT) of cast and printed specimens. Particularly, several microstructural investigation approaches that can evaluate specific pore structures are newly introduced for a better understanding of the material characteristics and properties of 3DPC. In addition, transport and durability properties, such as capillary water porosity, water sorptivity, freeze-thaw and thermal resistance, are examined and correlated to that of cast concrete. The thermal performance of 3DPC exposed to different temperatures up to 450 °C is evaluated. Finally, a comparison between the cast and printed specimen properties is established.

2. Materials and printing process

2.1. Materials

The primary cementitious materials used in this study were cement CEM II/A-M (S-LL) 52.5 N, fly ash and silica fume. The cement was obtained from Lafarge Cement, produced in the Kujawy cement plant in Poland. The fly ash used in the study was obtained from

the Dolna Odra power plant (Poland), while the silica fume came from the Mikrosilika Trade Company (Poland). River sand with a particle size < 2 mm, obtained from SKMS in Poland, was used as the fine aggregate. The chemical compositions of the binder components are presented in Table 1, while the particle size distribution of the dry materials is presented in Fig. 1. To ensure proper flowability of the mixture and in order to facilitate the printing process, a high performance polycarboxylate superplasticizer (Sika ViscoCrete 125) was applied in powder form.

2.2. Mixture composition and fresh properties

The mixture composition in this investigation was based on a design used by Federowicz et al. [26]. However, to improve the carbon footprint of the mixture, CEM I was replaced with CEM II/A-M (S-LL) 52.5 N. Fly ash and silica fume were used as supplementary cementitious materials (SCMs), resulting in 829 kg/m^3 of binder, in total. The 3D printable mixture composition used in this study is presented in Table 2.

The fresh properties of the mixes were first determined to verify their suitability for printing. The flow table test (based on EN 1015-3 [27]) was performed to determine the flowability of the mix; it achieved a flow of 155 ± 10 mm. This result is considered to be optimal for 3D printing with the applied device and concurs with other studies [26,28–30]. The compressive strength of the fresh mix was tested in a squeezing test [29]. The apparatus is presented in Fig. 2a. Displacement control was applied to the samples (h = 35 mm, d = 60 mm) at a continuous rate of 30 mm/min. This value was chosen to reflect a real-time printing process. Compressive strength was evaluated for a 50 % strain level (17.5 mm). The test was performed 15 min after adding water. The mixture achieved an average compressive strength of σ = 6.218 kPa (n = 3, std = 0.808, CoV = 13 %). The shear stress was determined using a manual shear vane. The apparatus, described in [31] and presented in Fig. 2b, is commonly used in soil testing. Due to its high measurement error and human factors, the method is used only as a preliminary evaluation of the suitability of a mix for 3D printing. The mix was tested 15 min after adding water. The average value of the shear stresses for the mix used was τ_f = 0.2 kPa (n = 3).

2.3. Mixing process and printing

2.3.1. Printing setup

The printing setup consisted of a computer-controlled gantry printer with a PFT Swing M pump, with a printable volume of 145 × 120 × 80 cm^3. The pump was connected through a 6 m long Ø1 inch hose. The hose ended with a nozzle. In order to print one- and three-layered specimens, two types of nozzles were used: 50 × 40 mm and 40 × 15 mm, respectively. In this study, a printing rates of 1000 mm/min and 3000 mm/min was used. The extrusion rate was adjusted to the printing speed. The setup is presented in Fig. 3.

2.3.2. Mixing and transport

The mixture was prepared in a standard 90 L concrete mixer, with a mixing speed of 60 rpm. The dry components were firstly mixed together for 60 s. Afterwards, water was gradually added to the dry components. Overall, the wet mixing procedure took t = 300 s, divided into two segments. The initial segment (t = 120 s) was paused at t = 60 s. The pause was used to check if all of the components had been properly mixed. After the pause, an additional t = 120 s of mixing was applied. The prepared mix was then transported manually to the pump and the process of printing was started.

For printing of the 3-layer samples (3 L), a 40 × 15 mm nozzle and 3000 mm/min printing rate was applied. For printing of the single layer samples (1 L), a 50 × 40 mm nozzle and 1000 mm/min printing rate was used, to ensure a similar mix extrusion rate. After printing, the samples were sprinkled with water and covered with foil for 24 h. All of the samples were prepared at room temperature T = 20 ± 2 °C and at a relative humidity RH = 60 %. The samples were stored in water T = 20 °C for curing, until the day of testing. Reference mold-cast samples, designated as C, were prepared in accordance with EN 196-1 [32]. Prior to mechanical strength testing, the surfaces of the printed specimens were cut to match the reference size of 40 × 40 × 160 mm^3.

Table 1
The chemical composition (major components) of binder materials.

Component [wt%]	CEM II 52.5 N	Fly ash	Silica fume
CaO	59.3	4.44	< d.l.*
SiO_2	19.7	52.2	91.1
Al_2O_3	5.2	24.9	0.26
Fe_2O_3	2.5	5.76	< d.l.*
K_2O	0.96	2.63	1.58
Na_2O	0.19	1.35	
Cl^-	0.052	0.003	< d.l.*
Other	12.1	8.72	7.06
Total	100	100	100

* Below detection limit.

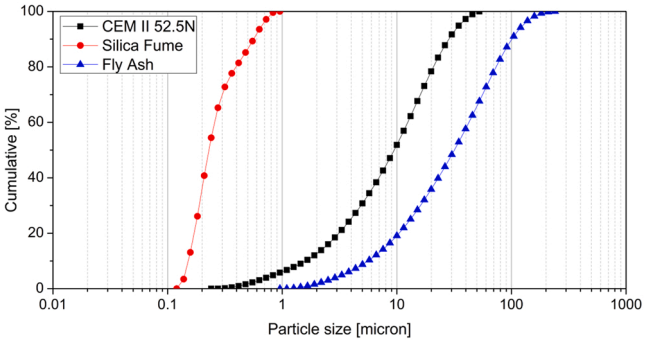

Fig. 1. Particle size distribution of binder materials.

Table 2
Composition of 3D printable mix [kg/m^3].

Sample designation	CEM II 52.5 N	Fly ash	Silica fume	Sand 0–2 mm	Water	Superplasticizer
3DPC	580	166	83	1270	200	2.0

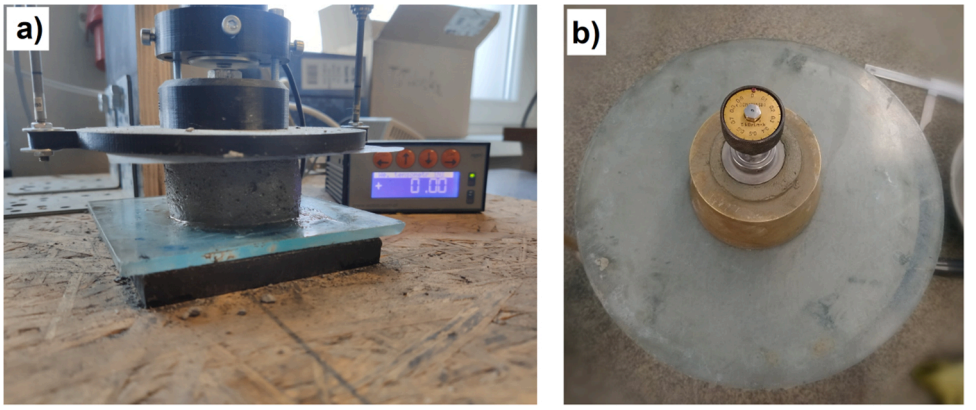

Fig. 2. Squeezing test (a) and shear vane (b) apparatus.

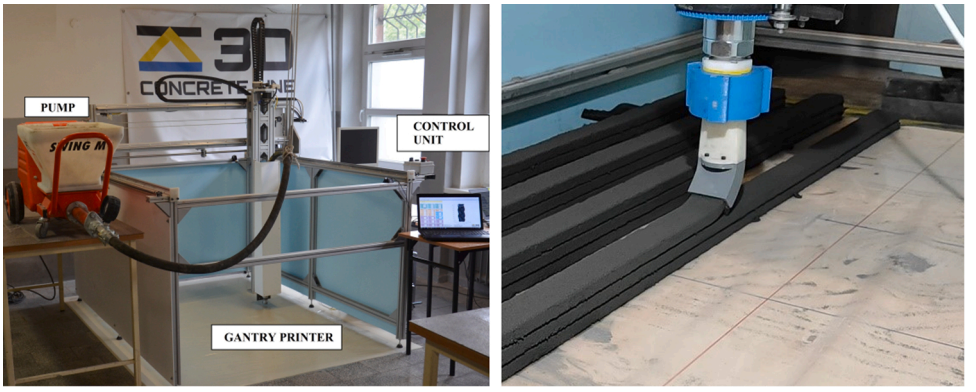

Fig. 3. Printing setup: gantry printer (left) and example of specimen printing (right).

3. Methods

3.1. Oven-dry density and transport properties

The oven-dry densities of the 3DPC specimens were measured after 28 d of curing, following EN 12390-7 [33]. Three specimens of each type were oven-dried at 105 °C until reaching a constant mass. The volume of the specimens was determined using a hydrostatic scale. The mean oven-dry density was then calculated. The water accessible porosity of the 3DPC was determined using a water displacement method. After 28 d of curing, the saturated mass of the specimens was determined, along with their submerged mass. Afterwards, the specimens were dried to a constant mass and weighed. Finally, the water accessible porosity was determined. Similarly to the oven-dry density, three specimens of each type of 3DPC were tested and the mean water accessible porosity value was taken as representative. The water absorption coefficient of the 3DPC was determined according to ISO 15148 [34], using the partial immersion method. To ensure one-directional water flow in the samples, three specimens of each 3DPC type were coated with paraffin wax. Afterwards, the specimens were weighed at selected time intervals and their sorptivity curves were determined. The water absorption coefficient was determined on the basis of these results.

3.2. Flexural and compressive strengths

Before the tests, the samples were taken out of the curing tank, surface dried, measured and weighed to assure correct results. Samples for the determination of flexural strength (40 ×40 × 160 mm^3) were placed in the testing machine (ToniTechnik 2 with a hydraulic press) and tested in accordance with EN 196-1 [32]. The samples were loaded at a constant rate of 50 N/s. Samples for the determination of compressive strength were acquired from the flexural strength tests, as halves of the prisms. These were loaded at a constant rate of 0.6 MPa/s. The strength determination was conducted after 1, 3, 7 and 28 d. The samples used for 28-day strength determination were tested in two perpendicular directions (D1 and D2). The samples prepared for the 1, 3, 7-day strength determination were tested in one direction (D1), as presented in Fig. 4.

3.3. Freeze-thaw resistance

For the freeze-thaw resistance (F-TR) determination, the test procedure was based on ASTM C666 [35]. The freezing and thawing protocol is presented in Fig. 5. Prior test, concrete samples with a size of 40 × 40 × 160 mm^3 were cured for 28 d. The weights of the specimens were recorded before and after the test. The strengths of the samples were determined after 25 and 50 cycles in the D1 direction, with changes in both the mass and strength determined.

3.4. Thermal performance

Thermal evaluations of 3PDC in the mid-temperature range (200 °C, 300 °C and 450 °C) were performed with the use of a muffle furnace. After 28 d of curing, specimens with a size of 40 × 40 × 160 mm^3 were dried for 24 h in an oven at 70 °C to remove excessive water, while reference (non-heated) samples were left in a climate chamber. The specimens were then exposed to elevated temperatures of 200 °C, 300 °C and 450 °C for 2 h, with a heating rate of 4 °C/min. After heating, the samples were cooled at an approximate cooling rate of 4 °C/min. Six 3DPC prism specimens were used for evaluating the compressive strength and mass loss at each temperature. The residual relative compressive strength, determined in the D1 direction, was calculated as the ratio between the compressive strengths of the heated specimens and those cured at room temperature.

3.5. Mercury intrusion porosimetry (MIP) and scanning electron microscopy (SEM)

After 28 days of curing, mercury intrusion porosimetry (MIP) tests were performed using Pascal 140 and 240 series mercury intrusion porosimeters (Thermo Scientific). The mercury density was 13.55 g/mL, the surface tension was measured as 0.48 N/m, while the selected contact angle was 140°. Prior to measurement, small-cored specimens were taken from the middle parts of both cast and printed specimens. In order to stop hydration, the specimens were immersed in isopropanol and then freeze-dried.

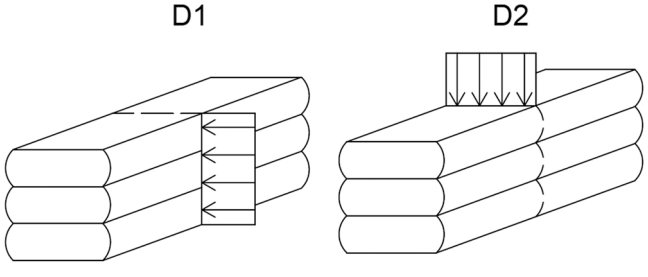

Fig. 4. Schematic illustration of specimen testing direction.

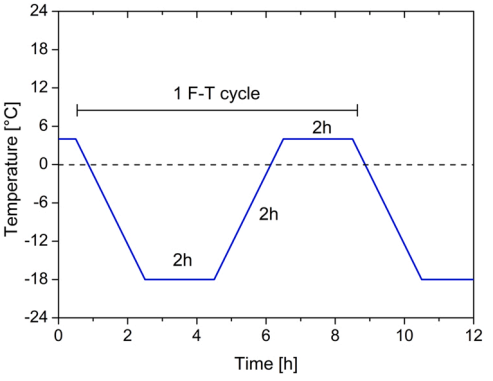

Fig. 5. Freeze-thaw cycle.

A low-vacuum scanning electron microscope, (SEM, Zeiss GeminiSEM500 NanoVP) was used to evaluate the microstructural properties of the specimens. 3DPC specimens were cut into slices along the sample height with a diamond saw and then polished. These were then freeze-dried in order to remove excess water.

3.6. Micro-CT evaluations

Micro-CT was used to examine the microstructures of the samples; pore structure in particular. Micro-CT is a non-invasive method which enables visualization of the inside of a sample [36–38], thus making it possible to identify the inner structures of the 3DPC specimens. For the measurement, a micro-CT device (Skyscan1173, Bruker, USA) was used. Fig. 6 shows the imaging procedure used to describe the pores and solid structures within a 3DPC specimen. Once a target specimen was scanned using X-rays, it was possible to obtain a series of reconstructed images which allowed microstructural investigation.

The 8-bit reconstructed image is expressed by 256 values between 0 and 255, with each value determined according to the relative density of the phase at a particular position. For example, the pores are described in black (value of 0), whereas the denser solids are described in a lighter color. For an effective investigation, a target component can be segmented and depicted as a binary image from the reconstructed image. A proper threshold needs to be selected in order to segment the phases, with a modified Otsu algorithm and manual selection [39] used for this purpose. In the binary image in Fig. 6, the white represents the pores within the reconstructed

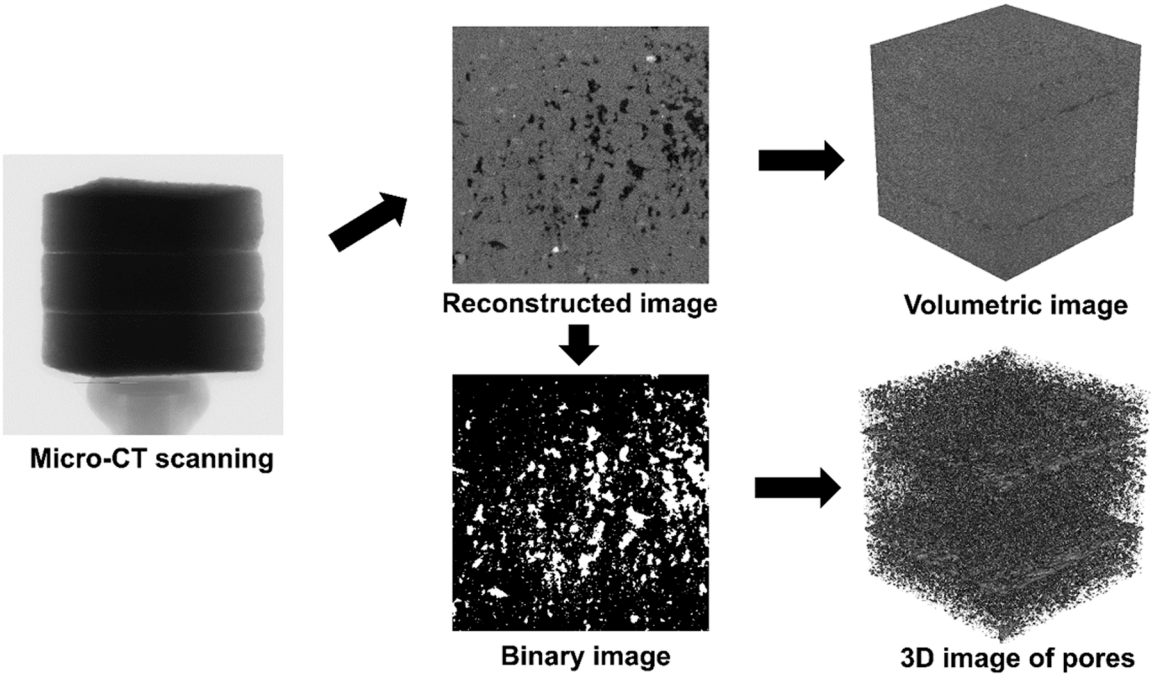

Fig. 6. Micro-CT imaging procedure used to obtain volumetric data (Note: in the binary image, the white represents pores within the specimen, while the black is the solid region).

image, while the black is the solid part. The volumetric information of a specimen can be obtained by subsequently stacking the reconstructed or binary images. The volumetric images in Fig. 6 show the solid and pore parts of the 3DPC samples, with the general features of both the solid and pore structures effectively described. This procedure was applied to all the samples under consideration, making it possible to examine the quantitative characteristics of the pores and solids – including pore size distribution, pore shape and relative solid density – using micro-CT generated images.

In general, the resolution of micro-CT images is strongly affected by specimen size. As such, increases in specimen size result in larger pixels and thus a less detailed image [40,41]. In contrast, the image resolution of a small sample is high, but the small sample is hard to be used as a representative volume element (RVE). To overcome these limitations, two specimen sizes for each case were used, to obtain a more detailed imaging measurement: $40 \times 40 \times 40$ mm^3 and $20 \times 20 \times 20$ mm^3 cubes, which were denoted as 'large' and 'small' samples, respectively. The images of the large samples were composed of 900×900 pixels (or voxels in 3D) with a voxel size of 29.78 μm, while the small sample images were expressed by 600×600 pixels with a voxel size of 19.94 μm. Both scale images were used to investigate the material characteristics of the 3DPC.

4. Results and discussion

4.1. Oven-dry density and transport properties

The results of oven-dry density, capillary water porosity and water absorption coefficient tests are presented in Table 3. No significant differences in the oven-dry densities of the specimens were found, regardless of the type of 3DPC preparation. A slightly higher oven-dry density value was reported for specimen 1L, although this value was within the expected deviation range. Evaluation of the capillary water porosity of the specimens showed that mold-cast (C) and 1-layer printed (1L) specimens exhibited similar values, while the 3L specimen exhibited one-fourth (8.16 %) higher water porosity than the mold-cast (6.46 %) specimen. This is attributable to additional inter-layer porosity, which increased the water absorption of the specimen during submersion in water. Fig. 7 presents the cross-sections of specimens after testing, confirming that water penetrated the specimen along the inter-layer connections; in the case of mold-cast and 1L specimens, water absorption was limited to the outer part of the specimen. In contrast, comparable water absorption coefficient values were observed for all the 3DPC specimen types. The water sorptivity test evaluates one directional water uptake, with the bottom part of a specimen submerged in water (Fig. 8). The water absorption coefficient is calculated based on specimens' water uptake within the first 24 h of the test. However, it was found that after 72 h the 3L specimen exhibited a higher water uptake than the 1-layer-printed and mold-cast specimens. Similarly to our work, a study on capillary water uptake evaluated by means of neutron radiography, carried out by Schröfl et al. [14], showed a noticeable rise in 3DPC capillary suction after longer time intervals, through the layer-to-layer interfaces. Moreover, it was found that moisture did not redistribute into other matrix regions from the interfaces, which confirms our observations during water porosity testing (Fig. 7).

4.2. Flexural and compressive strength

The results of flexural and compressive strength tests carried out after 1, 3, 7 and 28 d in the D1 testing direction, are presented in Fig. 9. Moreover, for comparison purposes, 28 d strengths were additionally determined in a perpendicular direction (D2).

No substantial differences between the flexural strengths values of the C and 1L specimens were detected, while a slightly lower flexural strength was observed for specimen 3L. 28 d flexural strength values for the 3L specimen, tested in both D1 and D2 directions, were 24 % and 27 % lower (respectively) than in the case of the C specimen. In contrast, lower compressive strength values were reported for both printed specimens, when compared to the mold-cast sample. After 28 days of curing, specimens 1L and 3L exhibited 20 % and 35 % lower compressive strengths than specimen C (respectively), when tested in the D1 direction and 24 % and 27 % lower (respectively) when tested in the D2 direction.

Various phenomena descriptions explaining the lower mechanical performance of 3D printed specimens, as compared to cast versions, are available in the literature. Printed specimens clearly exhibit anisotropic mechanical properties which depend on different loading directions; this being a result of the layered structure of printed elements. This in turn results in debonding and interface failure of layer connections. Therefore, depending on the testing direction, various phenomena – such as lateral deformation under vertical compressive loading – lead to decrements in specimens' mechanical performance. Moreover, depending on the printing pattern, voids and defects can occur, thus leading to a decrease in mechanical performance [30]. In our study no differences between the flexural strengths of the mold-cast and the 1L specimen were observed, although the specimen composed of 3 layers exhibited a lower flexural strength. A decrement in compressive strength has also been reported in other studies. For instance Lee et al. [42] reported approximately 30 % lower compressive strength for printed material, in comparison to cast material. However, in the work of Joh et al. [43]

Table 3
Oven-dry density, capillary water porosity and water absorption coefficients of 3DPC.

Sample designation	Oven-dry density [kg/m^3]	Capillary water porosity [vol%]	Water absorption coefficient [kg/ (m^2 h$^{0.5}$)]
C	2151 ± 22	6.46 ± 0.03	0.03042
1L	2196 ± 14	6.36 ± 0.32	0.03119
3L	2152 ± 26	8.16 ± 0.42	0.03439

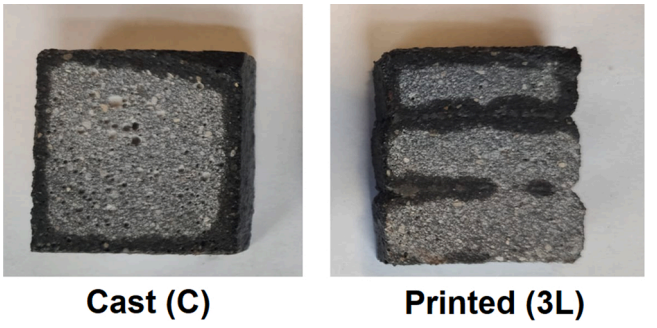

Fig. 7. Cross-section of C and 3L specimens after capillary water porosity tests (dark regions is water penetration depth).

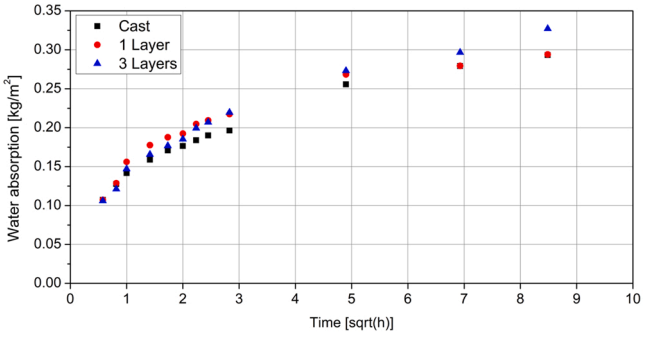

Fig. 8. Water uptake (up to 72 h) over the square root of time.

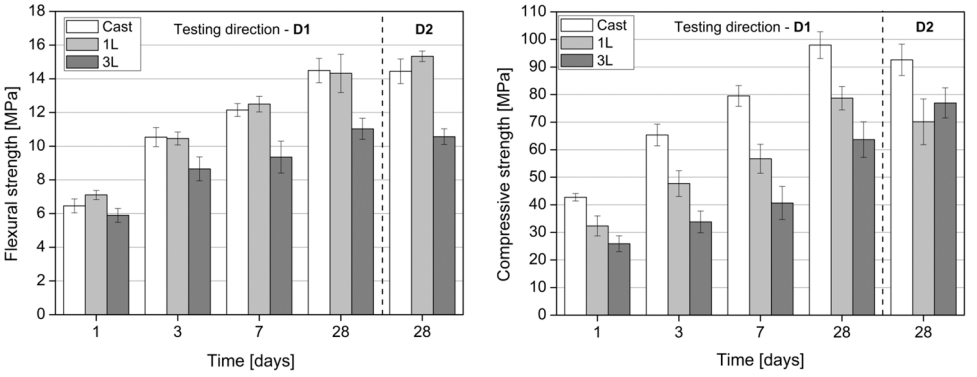

Fig. 9. Flexural (left) and compressive (right) strengths of 3DPC.

the difference did not exceed 15 %. They reported that the lower mechanical performance of printed specimens could be a result of cutting specimens, which results in potential micro-cracking and imperfection in the flatness of a specimen. Moreover, lower compressive strength can also be attributed to different curing conditions in the first 24 h after specimen preparation.

Mold-cast specimens are covered from all sides, thus ensuring humid conditions when 3D printed elements are exposed to air, which impairs the hydration process and thus affects compressive strength development; this was also found in the present study. The discrepancy between the compressive strength ratio of mold-cast and printed specimens, for up to 7 d of hydration, was significantly higher than after 28 d of curing. This effect was not observed in the case of flexural strength, as this value is not a reasonable indicator for evaluating the effectiveness of curing [44,45]. The results of this study show that only flexural strength varies minimally, with higher discrepancies observed for compressive strength. A similar observation was recently reported by Yang et al. [46], where the ratio between the flexural strength of cast and printed 28 d and 90 d cured specimens was almost 1, at both testing ages. Furthermore, the difference between the compressive strength of printed and cast specimens was found to have decreased after 90 days of curing, when compared to 28 d.

As reported by Lee et al. [42], the difference in the mechanical performance of 3DPC is attributable to the extrusion process, which results in different porosities between printed and cast specimens. The strength of their printed mortar was relatively low because the

inside was not as dense as in the case of the mold-cast mortar [42]. Similarly, Yu et al. [6] have reported slightly higher porosity for 3D printed specimens. In this study, total porosity values, as well as the pore size distributions of specimens, remained comparable to that of mold-cast specimens, but a difference in mechanical performance was reported. Previous studies carried out by Sikora et al. [19] and Chougan et al. [18] have confirmed the presence of anisotropic voids in 3DPC, which are known to have the potential to alternate the directional dependencies of strength. A similar phenomena was observed in the present study and is discussed below, in Section 4.6.

4.3. Freeze-thaw resistance

The results of freeze-thaw resistance tests are presented in Fig. 10. It is clear from the results that, after 25 and 50 F-T cycles, no significant compressive strength loss occurred in the specimens. In contrast, a slight strength reduction in flexural strength was found. After 25 F-T cycles, no differences in flexural strength loss, regardless of the type of specimen, were observed, with losses not exceeding 10 % of the initial strength. However, further strength decrements occurred after 50 F-T cycles, with the highest loss seen in the 3L specimen. This specimen exhibited 79 % of the initial flexural strength value, as compared to 89 % and 91 % reported for C and 1L, respectively. The proper resistance of specimens to freezing and thawing action can be explained by their low sorptivity (Table 3), which is an effect of the dense and homogenous microstructure, possible due to the high binder content and low w/b of the specimens.

A MIP study (Section 4.5) confirmed that the cement matrix of the 3DPC is composed mostly of fine pores (small capillary pores and gel pores), which are not affected during freezing and thawing action; as a result, the resistance of specimens was high. The higher flexural strength loss reported for the 3L specimen is attributable to the locally higher porosity in the inter-layer connection, confirmed by a micro-CT study (Section 4.6), which resulted in increased sorption of the specimen and weaker interfacial bonding. As is known, flexural strength is highly susceptible to internal defects (i.e. micro-cracks), meaning that, during testing, crack propagation and thus strength loss occur. To date, limited data related to the freezing-thawing resistance of 3DPC is available, but similar conclusions have recently been reported by Assaad et al. [47], showing that repeated F-T cycles weaken the interfaces along 3D printed mortar layers, leading to a substantial decrease in interfacial bonding strength after freezing-thawing testing.

4.4. Thermal resistance

The results of relative residual compressive strength tests and the mass loss of 3DPC specimens after exposure to elevated temperature is presented in Fig. 11. According to Neville et al. [48], concrete is generally highly resistant to temperatures of up to 300 °C, with only relatively minor damage occurring. Moreover, the damage is reversible through the so-called 're-hydration process'. Exposure to higher temperatures can be harmful to concrete, as severe processes resulting in decomposition of calcium hydroxide (CH) and Calcium-Silicate-Hydrates (C-S-H) gel occur [49]. However, the resistance of cementitious materials to mid-range temperatures (up to 300–450 °C) is of high importance in some applications, for example, nuclear power plants, where temperatures during emergency situations can reach up to 345 °C [50].

It is obvious that up to 300 °C, no significant changes in the mass loss of 3DPC specimens was found for any of the temperatures tested (Fig. 11). After exposure to 200 °C specimens exhibited a slight compressive strength reduction, which is most probably attributable to the evaporation of free water and the dehydration of ettringite and aluminosulphate hydrates. On the other hand, exposure to 300 °C resulted in a strength gain attributable to so-called 'autoclaving', which occurs in dense cementitious microstructures and speeds up the processing of unhydrated cement clinker; which in turn results in strength improvement [49].

After exposure to 450 °C, the prism (40 × 40 × 160 mm^3) specimens exhibited an explosive spalling effect, resulting in the loss of 3DPC integrity. As such, these specimens could not be used for further evaluation of mechanical performance. This effect is similar to that observed in cementitious composites with extremely dense microstructures, such as ultra-high performance concretes (UHPC) [51]. In contrary, small scale cubic specimens (sides of 2 cm), dedicated to micro-CT evaluations, resisted the heating process and were thus used for further investigations. After exposure to elevated temperatures, slightly higher relative residual compressive strength values were reported for 1L specimens, as compared to mold-cast ones, with 3L exhibiting the highest strength loss. This could be

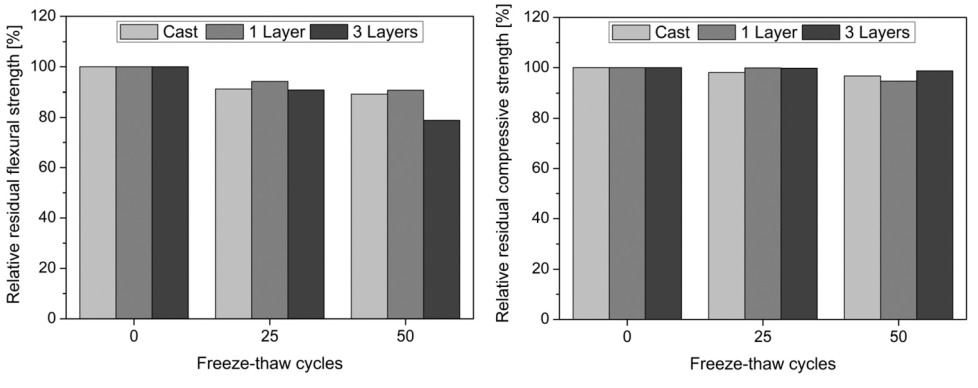

Fig. 10. Relative residual flexural (left) and compressive (right) strengths after 25 and 50 freeze-thaw cycles.

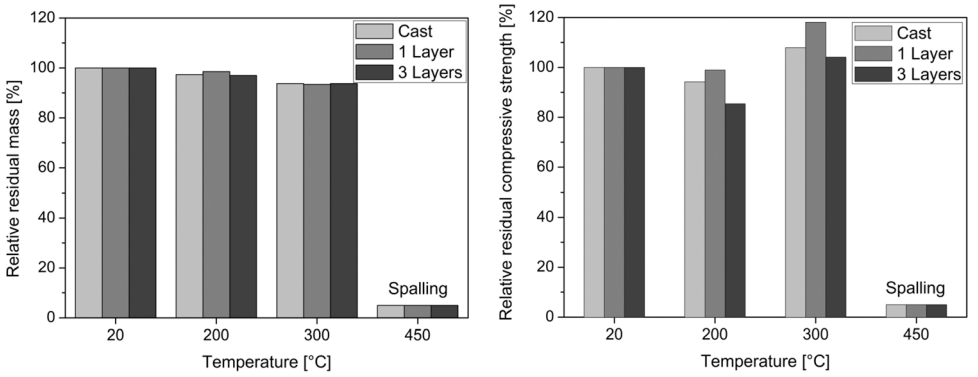

Fig. 11. Relative residual mass (left) and compressive strength (right) of specimens after exposure to elevated temperature.

attributed to weaker bonding between the layers, which deteriorates additionally during heating as a result of cement paste shrinkage, as well as because of a higher water evaporation rate from more porous areas.

The literature related to the thermal resistance of 3D printed cementitious composites is limited, as is the case in regard to freeze thaw resistance. However, Cicione et al. [52] have reported spalling of both mold-cast and printed specimens, as well as interlayer delamination of the latter, during heating (the temperature measured in the middle of the specimens reached 300 °C). In contrast, Xiao et al. [22] did not report any substantial differences in the strength values between mold-cast and printed specimens in temperature ranges comparable to those in the present study. However, they also reported spalling and inter-layer debonding after exposure to higher temperatures (600 °C and 800 °C). The effects of thermal exposure on the microstructural characteristics of 3DPC is presented in Section 4.6, below.

4.5. Mercury intrusion porosimetry

The results of MIP measurements are presented in Fig. 12 and Table 4. There are several methods of pore classifications available in the literature. In this study, pore classification was based partially on Mehta and Monteiro [53], where: d > 0.10 μm (more harmful pore), d = 0.05–0.10 μm (harmful pore), d = 0.0045–0.05 μm (less harmful pore), d < 0.0045 μm (harmless pore); with the suggestion that when d < 0.05 μm, pores exert less impact on strength and permeability. The volume of d > 20 μm pores was calculated in order to compare the results with micro-CT observations.

The MIP study showed that all the specimens tested exhibited relatively comparable porosities, with the highest value reported for the mold-cast specimen (8.16 %) and the lowest for the 3L specimen (6.70 %). In general, a very low 3DPC porosity, with low average and mean diameter, was observed (Table 4). The highest volume of less harmful pores (d < 0.05 μm) was found in specimen 1L (70 %), followed by 3L (63 %), while the highest contribution of harmful pores (d > 0.10 μm) occurred in the cast specimen. Moreover, a slightly higher contribution of larger voids > 20 μm was visible in the mold-cast specimen (4.5 %), as compared to 1L (3.72 %) and 3L (2.81 %), which will be discussed further in the following section. The results of the MIP study thus confirm the very low sorption characteristics (water sorptivity and capillary water porosity) of 3DPC, as discussed in previous sections, above. However, despite slight differences in the MIP results, it seems that the alteration of the pore structure had minor effects on transport properties, due to specimens' low total porosity which reduces the number of open channels for water transfer (connected pores). No substantial differences in the porosity between mold-cast and printed specimens were found in the present study. This can be attributed to binder composition and the substantially low w/b of the mixture design. A similar observation regarding pore structure was recently reported

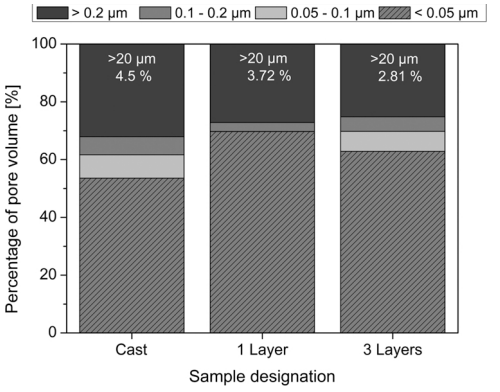

Fig. 12. Percentage of 3DPC pore distribution, as obtained by MIP.

Table 4
The results of MIP analysis of 3DPC.

Sample	Pore volume [g/cm^3]	Porosity by Hg intrusion [vol%]	Total pore surface area [m^2/g]	Average pore diameter [nm]	Median pore diameter [nm]
Cast	37.87	8.16	6.48	23.36	35.91
1 Layer	34.17	7.86	9.15	14.93	12.41
3 Layers	37.89	6.70	8.41	18.01	21.56

by Baz et al. [54], where slightly higher porosity was reported for mold-cast specimens than for printed ones. The authors attributed this phenomenon to the lack of vibration in 3D printed specimens. However, in contrast to the present study, the authors reported that non-printed specimens had a much higher number of tiny pores than printed specimens. Yu et al. [6] reported 13.3 % MIP porosity for mold-cast concrete with a w/b of 0.31, while the porosity of printed specimens was 23 %. It can therefore be concluded that porosity characteristics are highly dependent on the type of mixture composition used and the transport and extrusion process. Unlike typical casting methods, where concrete is placed into formwork and vibrated to remove entrapped air, 3DPC is pumped under pressure through a nozzle and so it does not experience extensive vibration before or after deposition. However, in our study the cast specimen exhibited a higher content of large spherical voids, which is attributable to low w/b and high mixture viscosity. This in turn resulted in entrapped air in the specimen and the creation of spherical voids, as confirmed by the micro-CT results (Section 4.6).

4.6. Micro-CT characterization

For a more detailed characterization of the 3DPC, micro-CT measurement was also conducted. Since pore structure is the most critical element in determining the material properties of cement-based materials, several pore characteristics were examined using

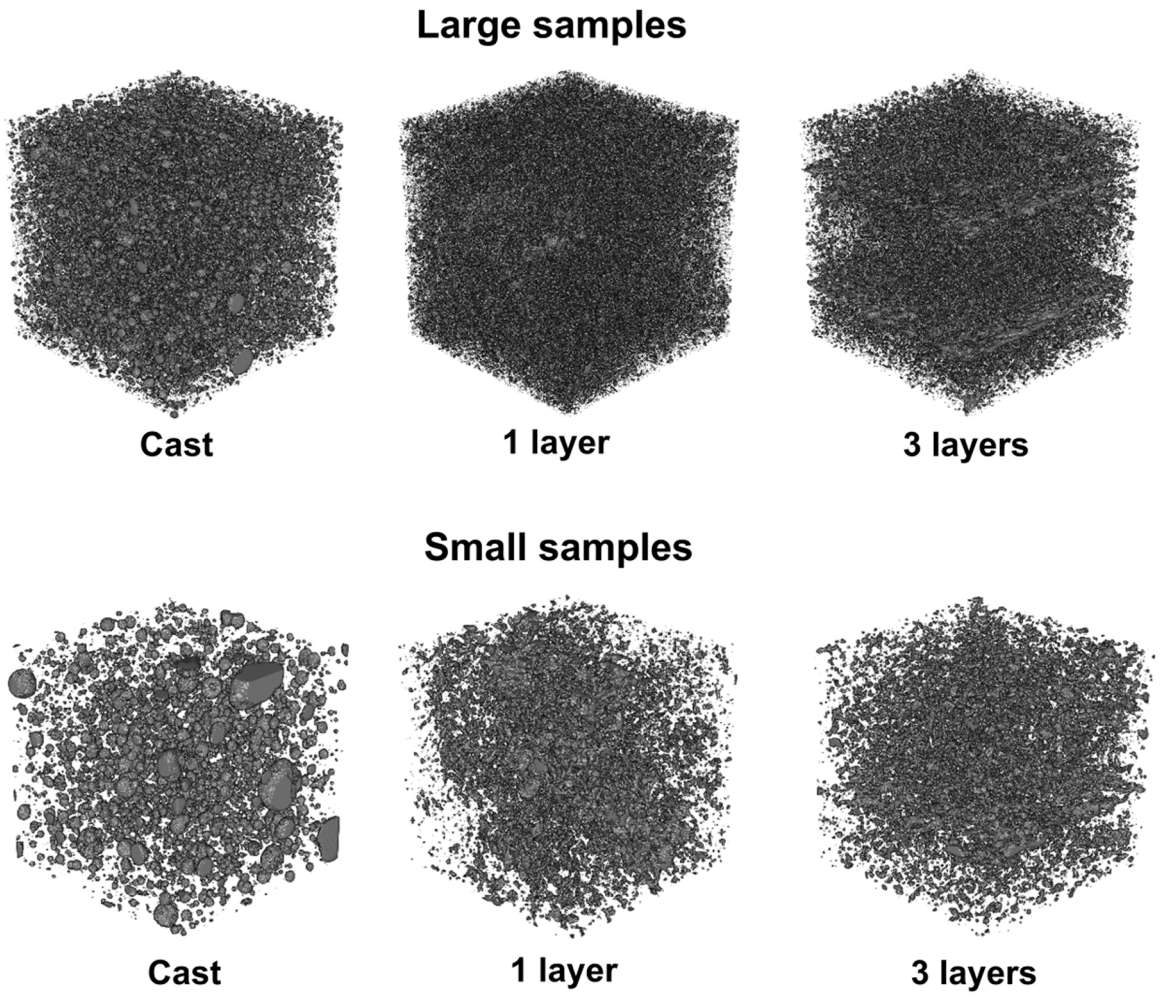

Fig. 13. Pore volume image in the samples studied (Note: the grey color denotes the pores within the specimens).

the micro-CT data. Fig. 13 shows the pore volume for each specimen type, for both large and small samples. Considering the image resolution of each scale, only pores larger than 30 μm were taken into consideration in the large samples, while only those larger than 20 μm were taken into consideration in the small samples.

The volumetric pore images make it possible to examine the general features of each specimen type. In the 3L specimen images, distinctly distributed pore layers were identified; these are assumed to be the connection between the layers. In contrast, the pores were dispersed uniformly in the Cast and 1L specimens, as anticipated. The porosity computed from the micro-CT data was 8.07 %, 5.10 %, and 5.09 % for larger C, 1L and 3L specimens, respectively. For the small samples, the computed porosity was 6.78 % (Cast), 6.01 % (1 layer) and 4.52 % (3 layers). In general, the trend of porosity in each specimen show consistency with the result of MIP, although the porosity values in each scale are smaller than those of the MIP, because the pore ranges measured by micro-CT and MIP were different. Among the samples studied, the Cast one showed higher porosity than the printed ones, which is consistent with the MIP result and other publications [54]. However, the differences in the number of pores between the Cast and printed specimen are not substantial and porosity itself might not be the only factor affecting material properties.

In addition to porosity, the pore size distribution of the samples was also evaluated. Fig. 14 shows the pore size distribution of each sample, for different scales. As shown in Fig. 14, the 3DPC specimen contained a higher number of smaller pores than the Cast sample, which concurs with the MIP results. Based on the pore size distribution, it can be seen that the printed specimens had a more homogeneous pore structure than the Cast specimen. The printed samples had a lower porosity and a higher proportion of small pores. However, a larger proportion of big pores cannot explain the differences in mechanical properties, because the Cast sample contained more large pores and had a higher porosity, but had higher overall strength, compared to the 3DPC. To explain these contradictions, a more detailed investigation of the pore structure was needed.

Fig. 15 shows the local porosity of the specimens, along with their height. The porosity was computed from the cross-section at each height. In the C and 1L samples, the porosity difference along the specimens was relatively small, meaning that the samples had generally uniform pore distribution. In the case of the 3L samples, regions with higher porosity were present along the interlayer connection zones, but besides this the samples had relatively uniform pore distributions. The results indicate that the bulky parts of all the specimen types were generally homogeneous, which confirms the quality of the produced elements. In the 3L samples for both large- and small-scale samples, the distinct regions, which assumed to be interlayers, show much higher porosity than the other parts due to the inconsistent quality of the material between the layers and the bulky part; this can be considered as a systematic problem of 3DPC that inevitably occurs during the printing process. The locally increased porosity of the multi-layer specimens can be a cause of the lower mechanical properties of the printed elements.

For an additional pore characterization, a probabilistic approach, the lineal-path function was also considered. The lineal-path function, L2, is a probability function that can describe the relative clustering of a specific phase and has been used to characterize cement-based composites [55,56]. The detailed description of the lineal-path function can be found in [56], and the result for the 3DPC is presented in Fig. 16. In this figure, the L2 results of each case for the pores is shown in the x, y, and z directions, where the z-axis is the direction of the specimen height. In the functions of the Cast and 1L specimens, the L2 functions for each direction tend to be similar, which indicates their isotropy. However, in 3L, the L2 function in the z-axis shows relatively lower than other directions, and this denotes that the pores in the z (height direction) are less clustered, in other words, thinner than other directions; this anisotropic characteristics obtained from the micro-CT data can attribute to the decrease of mechanical properties for a specific direction.

For a more detailed investigation of the pore structures of the specimens, the effect of pore shape was also examined quantitatively using micro-CT data. The pore shape itself can affect the mechanical properties significantly [57], but it is quite difficult to examine the

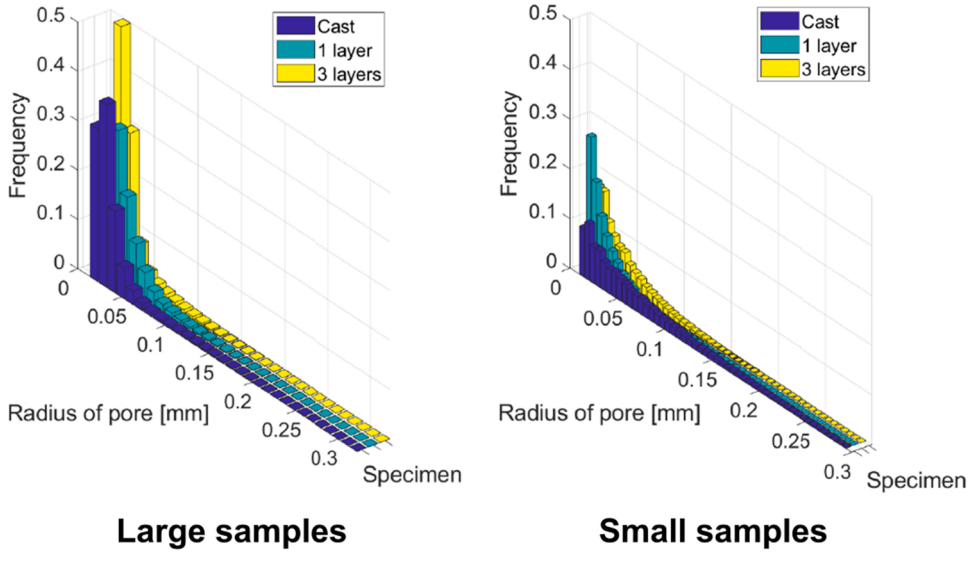

Fig. 14. Pore size distribution of the specimens (Note: in each size, only pores larger than the pixel sizes were taken into consideration).

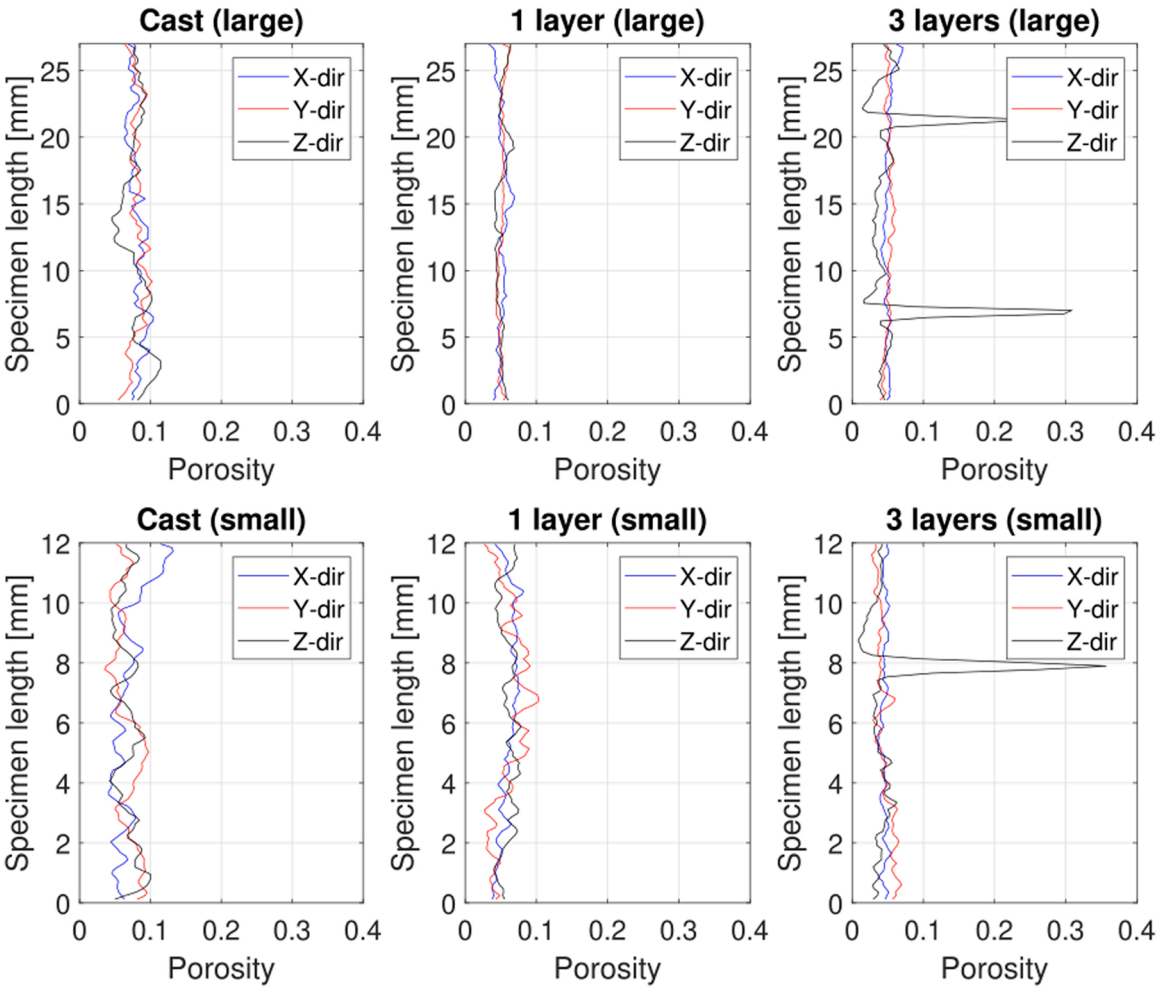

Fig. 15. Porosity distribution along specimen cross-section (Note: for large and small samples, only pores of about 26 mm and 12 mm in length, respectively, were taken into consideration, considering the region of interest (ROI) of the samples).

shape characteristics from experimental approaches. The pore data obtained from the micro-CT can be effectively utilized for this purpose, and here, Wadell's sphericity index was used to characterize the equiaxed shape degree, so as to evaluate pore shape [58]. Wadell's sphericity is defined as the ratio between the surface area of a target pore and the surface area of a sphere, with the same pore volume. Sphericity can have a value between 0 and 1, where 1 designates a completely spherical pore. Fig. 17 depicts the sphericity of pores in the samples studied. Compared to the Cast samples, 3DPC had a higher content of anisotropic pores with low sphericity, regardless of sample size. In particular, a distinct difference in the sphericity of the Cast and printed specimens was observed. In the case of the Cast samples, most of the pores had a sphericity larger than 0.6, while the 3DPC samples contained numerous pores with anisotropic pores; i.e. those having a sphericity lower than 0.4. In comparison between the large and small samples, the small samples tend to have larger sphericity values than the large samples, particularly in the 3L specimens. In the 3L specimen, as can be confirmed in Fig. 13, the large sample contains more interlayers than the small sample, and this contributes to the lower sphericity values because the interlayers tend to include a larger portion of anisotropic pores. These anisotropic pores might explain the reduction in the mechanical properties, such as compressive and flexural strength, of the materials [57]. Even though the 1L and C specimen had similar porosity and pore size distributions, the 1L specimen had a higher number of anisotropic pores, which decreased its compressive and flexural strength. In comparison of the 1L and 3L specimens, the 3L specimen contains more proportions of larger and anisotropic pores than the 1L case, which might affect the lower compressive strength. Anisotropic pores, generated during the printing procedure, might therefore cause a reduction in mechanical properties, compared to cast specimens. As such, the directional dependency of pores needs to be carefully considered in the printing process.

Fig. 18 shows the mean pixel value in relation to the height of each specimen to confirm the solid characteristics of the 3DPC. As discussed above, the pixel value of the image is determined according to the relative density of a particle. The mean pixel can represent the relative density at the position of the specimen [19]. In Fig. 18, despite small fluctuations, the maximum difference in the pixel values was less than 10 %, which confirms that the 1L and C samples were generally homogeneous. The 3L specimen exhibited lower

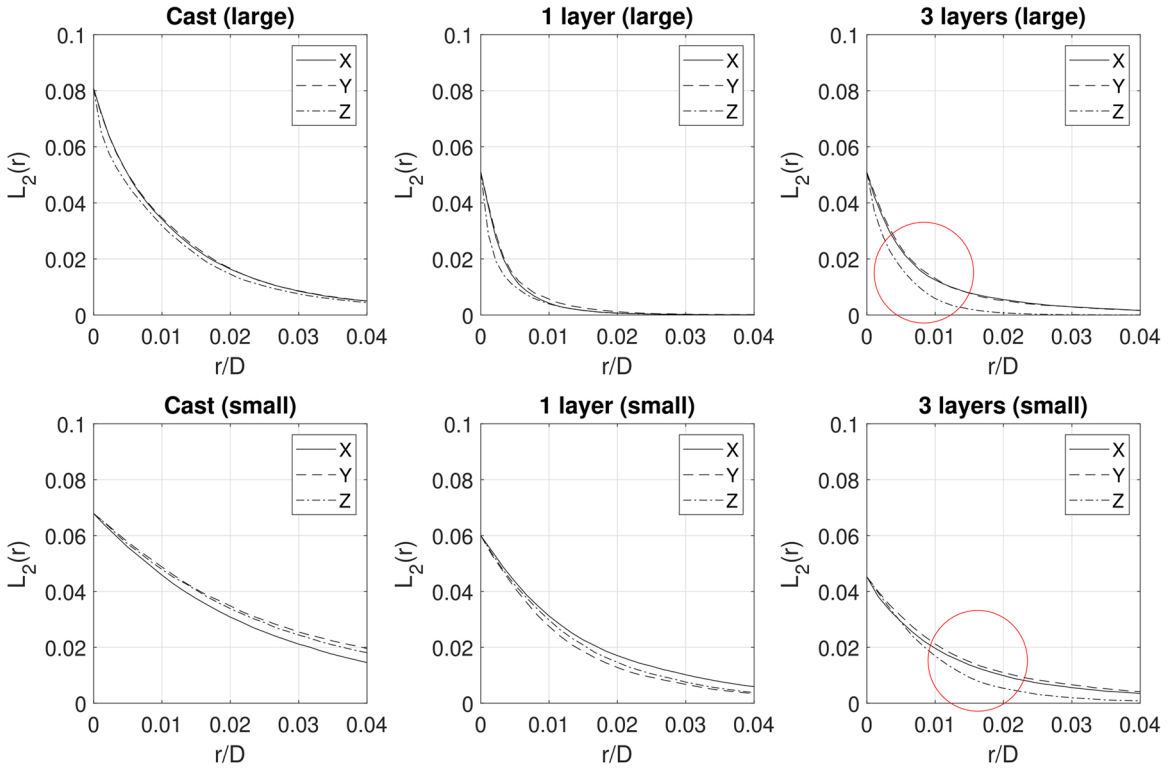

Fig. 16. Lineal-path function (L2) for the specimens in the x, y, and z directions (Note: in the considered direction, the z-axis is the direction of height. In each function, *D* is the specimen length, and *r* is the length of random line.).

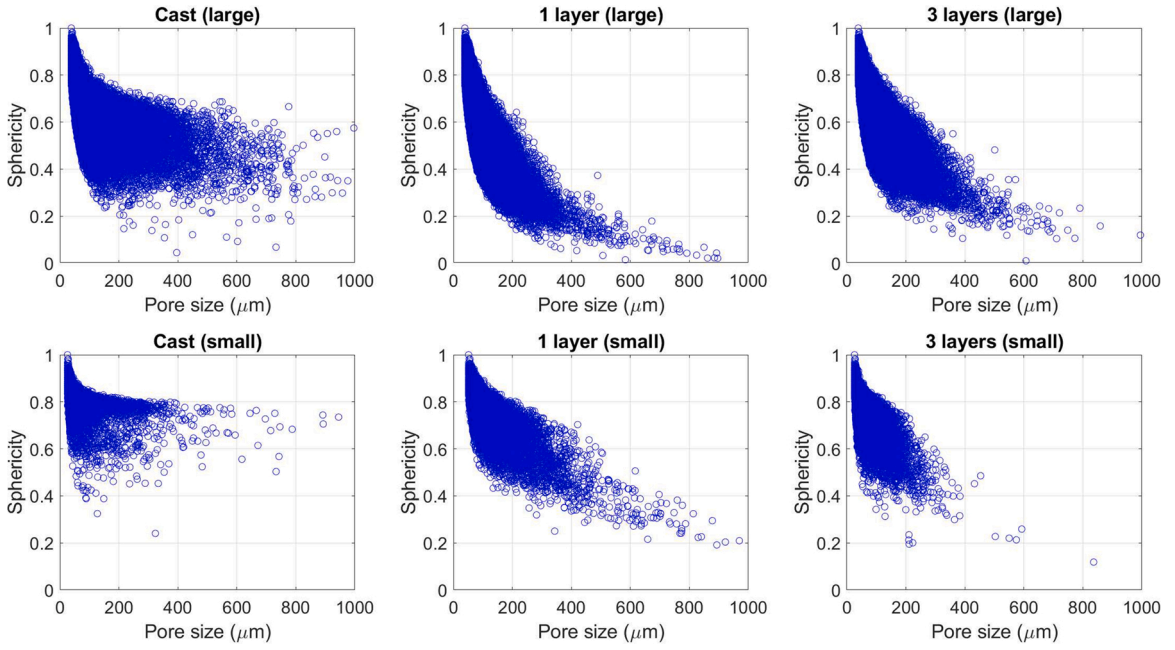

Fig. 17. Sphericity of pores within the specimens (Note: sphericity becomes 1 when a pore is completely spherical).

pixel values close to the interlayer zone, which contributed to lowered mechanical properties.

The effect of temperature was evaluated to confirm the stability of the samples produced. For this purpose, the pore structures of the specimens at 20 °C (reference), 200 °C, 300 °C and 450 °C were compared. Fig. 19 show the volumetric image at each temperature.

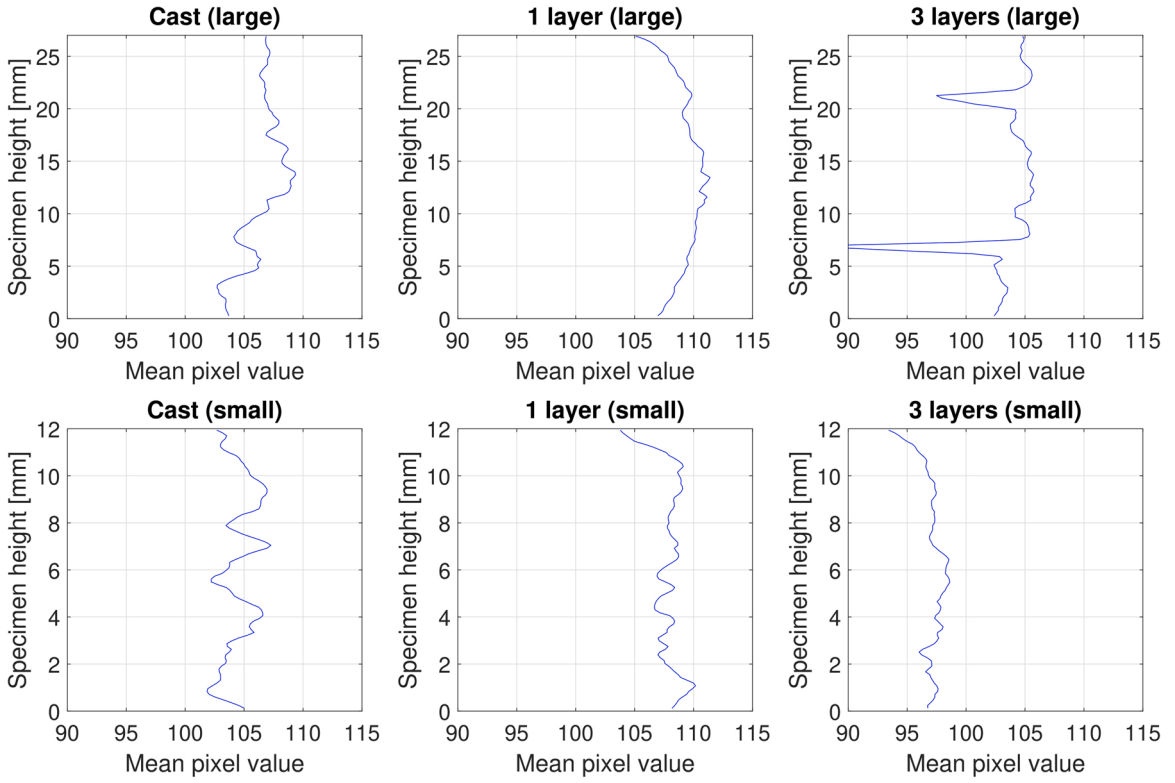

Fig. 18. Mean pixel value of the specimens, according to height.

The images were achieved using micro-CT imaging. The pore sizes under consideration remained the same as those of the specimens before heating. The data obtained shows that the differences in porosity, regardless of temperature, were almost insignificant between the samples and for the same sample type at different temperatures. In all cases, the increment of the total porosity of specimens did not exceed 5 %, which indicates that the produced samples were not influenced by temperatures up to 450 °C. However, as mentioned before, the obtained micro-CT here only concerned the pores larger than 20 μm, the difference in the smaller pores than the considered size, which might affect the mechanical and durability properties, needs to be considered separately.

Overall, the pore and solid structures obtained from the micro-CT imaging confirm that the 3DPC produced in this study showed performance comparable to that of the cast specimen. However, the microstructural characteristics of 3DPC show certain limitations, caused by anisotropic pores, which should be appropriately addressed properly in the future.

4.7. Scanning electron microscopy

The microstructures of the C, 1L and 3L specimens obtained by SEM are presented in Figs. 20–22. The micrographs confirm the results of the micro-CT studies regarding the type, size and sphericity of the pores. In general, a uniform, dense and compacted 3DPC microstructure, with distinguishable particles of fly ash and unreacted cement clinker, is visible in all specimens. Large spherical voids can be distinguished in the mold-cast C specimen (Fig. 20), which can be attributed to the specimen preparation method. High mix viscosity caused difficulties with proper specimen vibration. In contrast, anisotropic pores and spherical voids can easily be distinguished in the 3D printed specimens. In the 1L specimen, the voids were distributed uniformly and the pores had (Fig. 21a) lower diameters than those in the C specimen. Moreover, anisotropic voids were also visible (Fig. 21b–d). This confirms the findings the of micro-CT and MIP studies, showing that the cast specimen exhibited a slightly higher number of spherical voids with larger diameters. Similar microstructural features to that of the 1L specimen were found in specimen 3L. However, significantly higher porosity and anisotropic void contents were observed in the interlayer zone of the 3L specimens (Fig. 22c–d). As reported by [14], the weak interface between layers and quicker capillary suction through the layer-to-layer interfaces – which was discussed in the preceding sections – might be responsible for the specimens' lower mechanical performance. The length of the voids in the interlayer zone was significantly higher than the average pore size in the specimens' bulk region. This was also confirmed by the micro-CT study, which showed higher local porosity in the interlayer zone. The same phenomenon was recently reported by Yu et al. [6].

5. Conclusions

The main target of this work was to investigate the microstructural and durability characteristics of 3D printed concrete and to

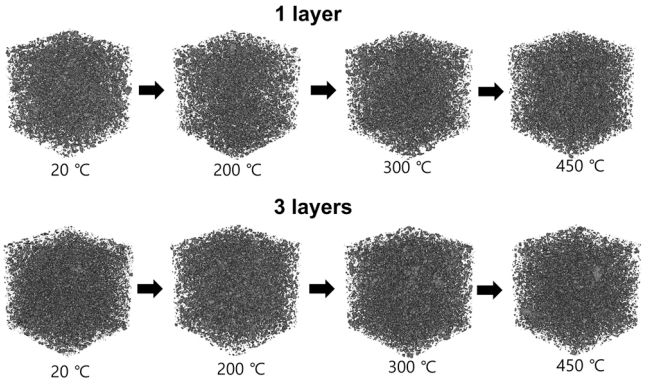

Fig. 19. 3D pore image of 3DPC specimens at different temperatures (note: the grey represents the pores within the samples).

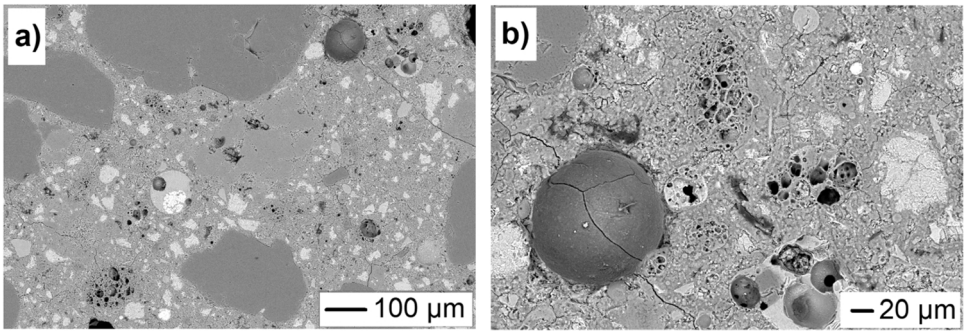

Fig. 20. SEM micrograph of mold-cast (C) specimen.

compare it with cast concrete. The following conclusions can be drawn from the results obtained:

1. 3 layer printed concrete exhibited lower density and a higher capillary water porosity and water absorption coefficient than both 1 layer printed and cast concrete, as a result of increased interlayer connection porosity. In general, the transport properties (capillary porosity and water sorptivity) of 3DPC were lower than in conventional concrete, regardless of whether the specimen was cast or printed.
2. Compared to cast concrete, 3D printed concrete had lower mechanical properties at all testing ages, with its mechanical performance exhibiting anisotropic behavior, thus being dependent on testing directions.
3. The performance of 3D printed concrete under freezing and thawing cycles, as well as in high temperature exposure up to 300 °C, was very similar to cast concrete and showed high stability. However, increasing the temperature up to 450 °C resulted in spalling behavior in all samples.
4. The total porosities of 3DPC, measured using MIP, were found to be very low due to the high binder content and low w/b ratio. Despite differences in pore size distribution between cast and 3D printed samples, their influence on absorption, freezing and thawing, as well as high temperature exposure resistance, were limited. However, during frost or thermal attack, the possibility of interlayer delamination in 3 layered printed specimens was present.
5. The pore and solid structures obtained by micro-CT imaging confirmed that the printed specimens exhibited differences in their pore size distributions and homogeneity, when compared to cast specimens. In general, printed concrete was found to be more homogenous in comparison to cast specimens, but microstructural features highlighted the limitations of the current materials, such as anisotropic pores and increased inter-layer porosity, which need to be overcome properly.
6. A new quantitative approach to evaluate the pore shape characteristics using micro-CT was introduced and demonstrated that the pore shapes were also affected by the production methods, and it affected the material properties.
7. SEM images showed increased interlayer porosity with anisotropic characteristic of 3D printed samples. In contrary, cast samples exhibited almost homogeneous distribution of voids with spherical shape.

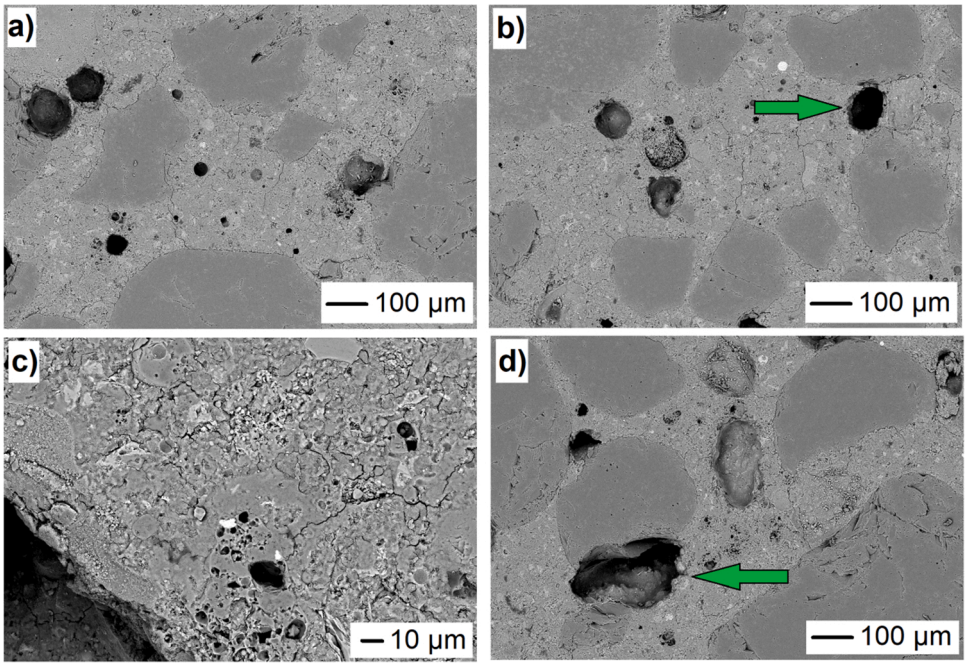

Fig. 21. SEM micrographs of 1 layer-printed (1L) specimen.

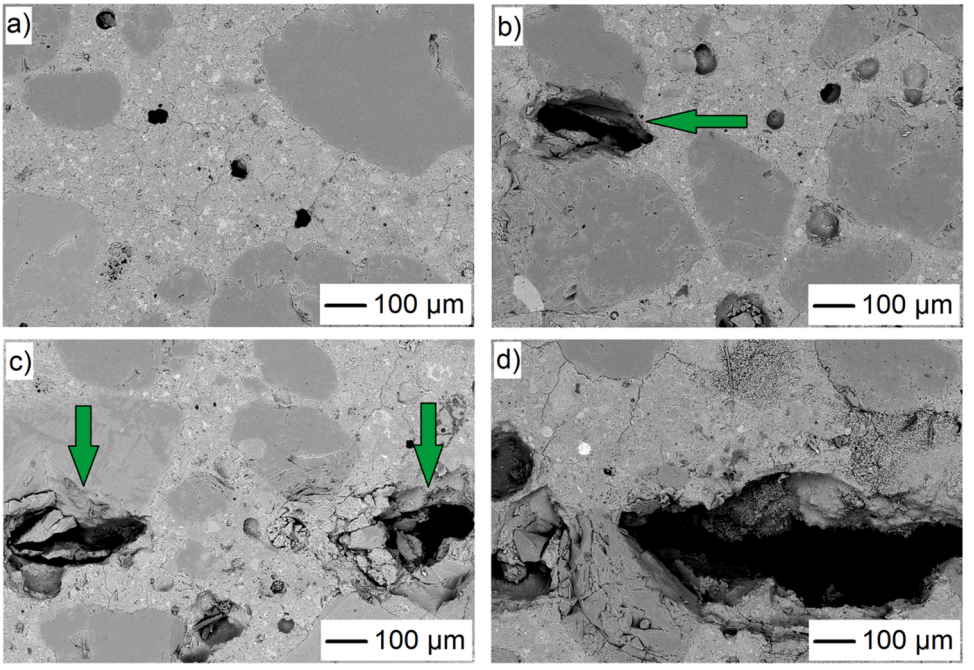

Fig. 22. SEM micrograph of 3-layer printed (3L) specimen: bulk phase (a,b) and interlayer connection (c,d).

Funding

This research was funded in part by the National Science Centre, Poland within Project no. 2020/39/D/ST8/00975 (SONATA-16).

CRediT authorship contribution statement

Pawel Sikora: Conceptualization, Methodology, Investigation, Validation, Visualization, Formal analysis, Data curation, Writing –

original draft, Writing – review & editing, Project administration, Funding acquisition, Supervision. **Mateusz Techman:** Conceptualization, Methodology, Resources, Investigation, Validation, Data curation, Visualization, Writing – original draft. **Karol Federowicz:** Conceptualization, Methodology, Investigation, Validation, Data curation, Visualization, Writing – original draft. **Ahmed M. El-Khayatt:** Investigation, Writing – original draft. **H. A. Saudi:** Investigation, Writing – original draft. **Mohamed Abd Elrahman:** Investigation, Validation, Writing – original draft, Writing – review & editing. **Marcin Hoffmann:** Methodology, Investigation, Validation, Resources, Writing – original draft. **Dietmar Stephan:** Methodology, Resources, Writing – review & editing. **Sang-Yeop Chung:** Conceptualization, Methodology, Investigation, Validation, Visualization, Formal analysis, Data curation, Writing – original draft, Writing – review & editing, Project administration, Funding acquisition.

Declaration of Competing Interest

The authors declare that they have no known competing financial interests or personal relationships that could have appeared to influence the work reported in this paper.

Data Availability

Data will be made available on request.

Acknowledgements

This work was supported by the National Research Foundation of Korea (NRF) grant funded by the Korea government (Ministry of Science and ICT, Grant no. NRF-2021R1A4A3030924).

The authors also would like to thank Francisco García-Moreno and Paul H. Kamm from Helmholtz Centre Berlin for fruitful cooperation and assistance in X-ray CT imaging. In addition, we would like to thank Christian Lehmann and David Dahncke from TU Berlin for their support with SEM and MIP measurements, respectively.

Data availability statement

The data presented in this study are available on request from the corresponding author.

References

[1] S.B. Balani, S.H. Ghaffar, M. Chougan, E. Pei, E. Şahin, Processes and materials used for direct writing technologies: a review, Results Eng. 11 (2021), 100257, https://doi.org/10.1016/j.rineng.2021.100257.
[2] J. Xiao, G. Ji, Y. Zhang, G. Ma, V. Mechtcherine, J. Pan, L. Wang, T. Ding, Z. Duan, S. Du, Large-scale 3D printing concrete technology: current status and future opportunities, Cem. Concr. Compos. 122 (2021), 104115, https://doi.org/10.1016/j.cemconcomp.2021.104115.
[3] S. El-Sayegh, L. Romdhane, S. Manjikian, A critical review of 3D printing in construction: benefits, challenges, and risks, Arch. Civ. Mech. Eng. 20 (2020), https://doi.org/10.1007/s43452-020-00038-w.
[4] P. Sikora, M. Chougan, K. Cuevas, M. Liebscher, V. Mechtcherine, S.H. Ghaffar, M. Liard, D. Lootens, P. Krivenko, M. Sanytsky, D. Stephan, The effects of nano- and micro-sized additives on 3D printable cementitious and alkali-activated composites: a review, Appl. Nanosci. (2021), https://doi.org/10.1007/s13204-021-01738-2.
[5] C. Zhang, V.N. Nerella, A. Krishna, S. Wang, Y. Zhang, V. Mechtcherine, N. Banthia, Mix design concepts for 3D printable concrete: a review, Cem. Concr. Compos. 122 (2021), 104155, https://doi.org/10.1016/j.cemconcomp.2021.104155.
[6] S. Yu, M. Xia, J. Sanjayan, L. Yang, J. Xiao, H. Du, Microstructural characterization of 3D printed concrete, J. Build. Eng. 44 (2021), 102948, https://doi.org/10.1016/j.jobe.2021.102948.
[7] J. Kruger, A. Du Plessis, G. van Zijl, An investigation into the porosity of extrusion-based 3D printed concrete, Addit. Manuf. 37 (2021), 101740, https://doi.org/10.1016/j.addma.2020.101740.
[8] M. Moini, J. Olek, J.P. Youngblood, B. Magee, P.D. Zavattieri, Additive manufacturing and performance of architectured cement-based materials, Adv. Mater. 30 (2018), e1802123, https://doi.org/10.1002/adma.201802123.
[9] V.N. Nerella, S. Hempel, V. Mechtcherine, Effects of layer-interface properties on mechanical performance of concrete elements produced by extrusion-based 3D-printing, Constr. Build. Mater. 205 (2019) 586–601, https://doi.org/10.1016/j.conbuildmat.2019.01.235.
[10] Y.W.D. Tay, G.H.A. Ting, Y. Qian, B. Panda, L. He, M.J. Tan, Time gap effect on bond strength of 3D-printed concrete, Virtual Phys. Prototyp. 14 (2019) 104–113, https://doi.org/10.1080/17452759.2018.1500420.
[11] J. van der Putten, M. Deprez, V. Cnudde, G. de Schutter, K. van Tittelboom, Microstructural characterization of 3D printed cementitious materials, Materials 12 (2019), https://doi.org/10.3390/ma12182993.
[12] S. Skibicki, M. Pułtorak, M. Kaszyńska, M. Hoffmann, E. Ekiert, D. Sibera, The effect of using recycled PET aggregates on mechanical and durability properties of 3D printed mortar, Constr. Build. Mater. 335 (2022), 127443, https://doi.org/10.1016/j.conbuildmat.2022.127443.
[13] J. van der Putten, M. de Volder, P. van den Heede, G. de Schutter, K. van Tittelboom, 3D printing of concrete: the influence on chloride penetration, in: F.P. Bos, S.S. Lucas, R.J.M. Wolfs, T.A.M. Salet (eds.), Second RILEM International Conference on Concrete and Digital Fabrication, Springer International Publishing, Cham, 2020, pp. 500–7.
[14] C. Schröfl, V.N. Nerella, V. Mechtcherine, Capillary Water Intake by 3D-printed concrete visualised and quantified by neutron radiography, in: T. Wangler, R.J. Flatt (eds.), First RILEM International Conference on Concrete and Digital Fabrication – Digital Concrete 2018, Springer International Publishing, Cham, 2019, pp. 217–24.
[15] J. Strzałkowski, H. Garbalińska, Usefulness of mercury porosimetry to assess the porosity of cement composites with the addition of aerogel particles, in: I.B. Valente, A. Ventura Gouveia, S.S. Dias (eds.), Proceedings of the 3rd RILEM Spring Convention and Conference (RSCC 2020), Springer International Publishing, Cham, 2021, pp. 411–23.
[16] P. Sikora, T. Rucinska, D. Stephan, S.-Y. Chung, M. Abd Elrahman, Evaluating the effects of nanosilica on the material properties of lightweight and ultra-lightweight concrete using image-based approaches, Constr. Build. Mater. 264 (2020), 120241, https://doi.org/10.1016/j.conbuildmat.2020.120241.
[17] S.-Y. Chung, J.-S. Kim, P.H. Kamm, D. Stephan, T.-S. Han, M. Abd Elrahman, Pore and solid characterizations of interfacial transition zone of mortar using microcomputed tomography images, J. Mater. Civ. Eng. 33 (2021), 4021348, https://doi.org/10.1061/(ASCE)MT.1943-5533.0003986.

[18] M. Chougan, S.H. Ghaffar, P. Sikora, S.-Y. Chung, T. Rucinska, D. Stephan, A. Albar, M.R. Swash, Investigation of additive incorporation on rheological, microstructural and mechanical properties of 3D printable alkali-activated materials, Mater. Des. 202 (2021), 109574, https://doi.org/10.1016/j.matdes.2021.109574.
[19] P. Sikora, S.-Y. Chung, M. Liard, D. Lootens, T. Dorn, P.H. Kamm, D. Stephan, M. Abd Elrahman, The effects of nanosilica on the fresh and hardened properties of 3D printable mortars, Constr. Build. Mater. 281 (2021), 122574, https://doi.org/10.1016/j.conbuildmat.2021.122574.
[20] L. Kong, M. Ostadhassan, X. Hou, M. Mann, C. Li, Microstructure characteristics and fractal analysis of 3D-printed sandstone using micro-CT and SEM-EDS, J. Pet. Sci. Eng. 175 (2019) 1039–1048, https://doi.org/10.1016/j.petrol.2019.01.050.
[21] Y. Chen, S. Chaves Figueiredo, Z. Li, Z. Chang, K. Jansen, O. Çopuroğlu, E. Schlangen, Improving printability of limestone-calcined clay-based cementitious materials by using viscosity-modifying admixture, Cem. Concr. Res. 132 (2020), 106040, https://doi.org/10.1016/j.cemconres.2020.106040.
[22] J. Xiao, N. Han, L. Zhang, S. Zou, Mechanical and microstructural evolution of 3D printed concrete with polyethylene fiber and recycled sand at elevated temperatures, Constr. Build. Mater. 293 (2021), 123524, https://doi.org/10.1016/j.conbuildmat.2021.123524.
[23] A.R. Arunothayan, B. Nematollahi, R. Ranade, S.H. Bong, J.G. Sanjayan, K.H. Khayat, Fiber orientation effects on ultra-high performance concrete formed by 3D printing, Cem. Concr. Res. 143 (2021), 106384, https://doi.org/10.1016/j.cemconres.2021.106384.
[24] G. Bai, L. Wang, G. Ma, J. Sanjayan, M. Bai, 3D printing eco-friendly concrete containing under-utilised and waste solids as aggregates, Cem. Concr. Compos. 120 (2021), 104037, https://doi.org/10.1016/j.cemconcomp.2021.104037.
[25] Y. Chen, O. Çopuroğlu, C. Romero Rodriguez, F.F. de Mendonca Filho, E. Schlangen, Characterization of air-void systems in 3D printed cementitious materials using optical image scanning and X-ray computed tomography, Mater. Charact. 173 (2021), 110948, https://doi.org/10.1016/j.matchar.2021.110948.
[26] K. Federowicz, M. Kaszyńska, A. Zieliński, M. Hoffmann, Effect of curing methods on shrinkage development in 3D-printed concrete, Materials 13 (2020), https://doi.org/10.3390/ma13112590.
[27] EN 1015-3 – Methods of test for mortar for masonry – Part 3: Determination of consistence of fresh mortar.
[28] Y.W.D. Tay, Y. Qian, M.J. Tan, Printability region for 3D concrete printing using slump and slump flow test, Compos. Part B: Eng. 174 (2019), 106968, https://doi.org/10.1016/j.compositesb.2019.106968.
[29] M. Kaszyńska, S. Skibicki, M. Hoffmann, 3D concrete printing for sustainable construction, Energies 13 (2020) 6351, https://doi.org/10.3390/en13236351.
[30] K. Cuevas, M. Chougan, F. Martin, S.H. Ghaffar, D. Stephan, P. Sikora, 3D printable lightweight cementitious composites with incorporated waste glass aggregates and expanded microspheres – rheological, thermal and mechanical properties, J. Build. Eng. 44 (2021), 102718, https://doi.org/10.1016/j.jobe.2021.102718.
[31] M. Hoffmann, S. Skibicki, P. Pankratow, A. Zieliński, M. Pajor, M. Techman, Automation in the construction of a 3D-printed concrete wall with the use of a lintel gripper, Materials 13 (2020), https://doi.org/10.3390/ma13081800.
[32] EN 196-1 – Methods of testing cement – Part 1: Determination of strength.
[33] EN 12390-7 – Testing hardened concrete – Part 7: Density of hardened concrete.
[34] ISO 15148 – Hygrothermal performance of building materials and products — Determination of water absorption coefficient by partial immersion.
[35] ASTM C666 – Standard Test Method for Resistance of Concrete to Rapid Freezing and Thawing.
[36] N. Bossa, P. Chaurand, J. Vicente, D. Borschneck, C. Levard, O. Aguerre-Chariol, J. Rose, Micro- and nano-X-ray computed-tomography: a step forward in the characterization of the pore network of a leached cement paste, Cem. Concr. Res. 67 (2015) 138–147, https://doi.org/10.1016/j.cemconres.2014.08.007.
[37] S.-Y. Chung, J.-S. Kim, D. Stephan, T.-S. Han, Overview of the use of micro-computed tomography (micro-CT) to investigate the relation between the material characteristics and properties of cement-based materials, Constr. Build. Mater. 229 (2019), 116843, https://doi.org/10.1016/j.conbuildmat.2019.116843.
[38] S.-Y. Chung, M.A. Elrahman, D. Stephan, P.H. Kamm, Investigation of characteristics and responses of insulating cement paste specimens with Aer solids using X-ray micro-computed tomography, Constr. Build. Mater. 118 (2016) 204–215, https://doi.org/10.1016/j.conbuildmat.2016.04.159.
[39] S.-Y. Chung, P. Sikora, D. Stephan, M. Abd Elrahman, The effect of lightweight concrete cores on the thermal performance of vacuum insulation panels, Materials 13 (2020), https://doi.org/10.3390/ma13112632.
[40] E. Gallucci, K. Scrivener, A. Groso, M. Stampanoni, G. Margaritondo, 3D experimental investigation of the microstructure of cement pastes using synchrotron X-ray microtomography (μCT, Cem. Concr. Res. 37 (2007) 360–368, https://doi.org/10.1016/j.cemconres.2006.10.012.
[41] Y. Yang, Y. Zhang, W. She, Z. Wu, Z. Liu, Y. Ding, Nondestructive monitoring the deterioration process of cement paste exposed to sodium sulfate solution by X-ray computed tomography, Constr. Build. Mater. 186 (2018) 182–190, https://doi.org/10.1016/j.conbuildmat.2018.07.145.
[42] H. Lee, J.-H.J. Kim, J.-H. Moon, W.-W. Kim, E.-A. Seo, Evaluation of the mechanical properties of a 3D-printed mortar, Materials 12 (2019), https://doi.org/10.3390/ma12244104.
[43] C. Joh, J. Lee, T.Q. Bui, J. Park, I.-H. Yang, Buildability and mechanical properties of 3D printed concrete, Materials 13 (2020), https://doi.org/10.3390/ma13214919.
[44] A. Zhang, W. Yang, Y. Ge, P. Liu, Effect of nanomaterials on the mechanical properties and microstructure of cement mortar under low air pressure curing, Constr. Build. Mater. 249 (2020), 118787, https://doi.org/10.1016/j.conbuildmat.2020.118787.
[45] D. Ye, D. Zollinger, S. Choi, M. Won, Literature Review of Curing in Portland Cement Concrete Pavement, Technical Report – FHWA/TX06/0-5106-1 – Center for Transportation Research, The University of Texas at Austin, USA, 2006.
[46] H. Yang, W. Li, Y. Che, 3D printing cementitious materials containing nano-CaCO3: workability, strength, and microstructure, Front. Mater. 7 (2020) 260, https://doi.org/10.3389/fmats.2020.00260.
[47] J.J. Assaad, F. Hamzeh, B. Hamad, Qualitative assessment of interfacial bonding in 3D printing concrete exposed to frost attack, Case Stud. Constr. Mater. 13 (2020), e00357, https://doi.org/10.1016/j.cscm.2020.e00357.
[48] A.M. Neville, J.J. Brooks. Concrete Technology, 2nd edition, Pearson, UK, 2010.
[49] P. Sikora, M. Abd Elrahman, D. Stephan, The influence of nanomaterials on the thermal resistance of cement-based composites–a review, Nanomaterials 8 (2018), https://doi.org/10.3390/nano8070465.
[50] ASME , Boiler and Pressure Vessel Code Section III – Rules for Construction of Nuclear Facility Components Division 2 – Code for Concrete Containments, American Society of Mechanical Engineers, 2007.
[51] F. Lo Monte, R. Felicetti, C. Rossino, Fire spalling sensitivity of high-performance concrete in heated slabs under biaxial compressive loading, Mater. Struct. 52 (2019), https://doi.org/10.1617/s11527-019-1318-0.
[52] A. Cicione, J. Kruger, R.S. Walls, G. van Zijl, An experimental study of the behavior of 3D printed concrete at elevated temperatures, Fire Saf. J. 120 (2021), 103075, https://doi.org/10.1016/j.firesaf.2020.103075.
[53] P.K. Mehta, P.J.M. Monteiro. Concrete: Microstructure, Properties, and Materials, McGraw-Hill, New York, USA, 2006.
[54] B. Baz, G. Aouad, J. Kleib, D. Bulteel, S. Remond, Durability assessment and microstructural analysis of 3D printed concrete exposed to sulfuric acid environments, Constr. Build. Mater. 290 (2021), 123220, https://doi.org/10.1016/j.conbuildmat.2021.123220.
[55] Torquato Lu, Lineal-path function for random heterogeneous materials, Phys. Rev. A 45 (1992) 922–929, https://doi.org/10.1103/PhysRevA.45.922.
[56] S.-Y. Chung, M. Abd Elrahman, D. Stephan, The effects of anisotropic insulations with different spatial distributions on material properties of mortar specimens, Int. J. Concr. Struct. Mater. 11 (2017) 573–584, https://doi.org/10.1007/s40069-017-0218-3.
[57] S.-Y. Chung, D. Stephan, M.A. Elrahman, T.-S. Han, Effects of anisotropic voids on thermal properties of insulating media investigated using 3D printed samples, Constr. Build. Mater. 111 (2016) 529–542, https://doi.org/10.1016/j.conbuildmat.2016.02.165.
[58] J.W. Bullard, E.J. Garboczi, Defining shape measures for 3D star-shaped particles: sphericity, roundness, and dimensions, Powder Technol. 249 (2013) 241–252, https://doi.org/10.1016/j.powtec.2013.08.015.